Three times accelerated glacier area loss in Svalbard revealed by deep learning

Konstantin A. Maslov[1,*], Thomas Schellenberger[2], Claudio Persello[1], Alfred Stein[1]

[1] Department of Earth Observation Science, Faculty of Geo-information Science and Earth Observation (ITC), University of Twente, Drienerlolaan 5, 7522NB Enschede, Overijssel, The Netherlands
[2] Department of Geosciences, Faculty of Mathematics and Natural Sciences, University of Oslo, Sem Sælands vei 1, Blindern, 0371 Oslo, Østlandet, Norway
* email: k.a.maslov@utwente.nl.

Abstract

The rapid warming in polar regions highlights the need to monitor climate change impacts such as glacier retreat and related global sea level rise. Glacier area is an essential climate variable but its tracking is complicated by the labour-intensive manual digitisation of satellite imagery. Here we introduce ICEmapper, a deep learning model that maps glacier outlines from Sentinel-1 time series with accuracy on par with human experts. We used this model to retrieve Svalbard glacier outlines for 2016–2024 and found a tripling of the glacier area loss rate in the last decade ($-227\,\mathrm{km^2\,a^{-1}}$) as compared to that of 1970–2006 ($-68\,\mathrm{km^2\,a^{-1}}$). Our analysis shows significant area changes related to glacier surging, namely, the Nathorstbreen system and Austfonna, Basin-3 surges. These two surges collectively added to the area change in 2006–2016 ($+194.30\,\mathrm{km^2}$ or $+0.60\%$), thus delaying the regionwide area loss by two–three years. In contrast, during 2016–2024, surging glaciers showed statistically significantly faster area loss rates than non-surging glaciers. Our results indicate a significant acceleration in glacier area loss in Svalbard, and we anticipate broader applications of our method to track glacier changes on larger scales.

Introduction

Glaciers serve as crucial indicators of climate change, providing valuable insights into environmental shifts due to the sensitivity to temperature and precipitation changes [1–5]. The Arctic region is experiencing rapid warming known as Arctic amplification, where temperatures are rising nearly four times faster than the global average [6]. This accelerated warming is particularly evident in regions like Svalbard [7], an Arctic archipelago where glaciers cover approximately 57% of the land area [8]. The rapid changes observed in Svalbard glaciers make it a critical zone for understanding climate processes and their impacts on polar environments [9–12].

The Global Climate Observing System (GCOS) recognises "glacier area" as one of the essential climate variables, but the recommended decadal-scale monitoring standards are rarely met [13]. In addition, traditional glacier monitoring methods, relying on optical satellite imagery, often suffer from limited temporal resolution due to cloud cover at the end of the ablation season when landscapes are free of seasonal snow [14]. In Svalbard, a point estimate of the glacier area loss rate of $\approx -80\,\mathrm{km^2\,a^{-1}}$ was reported for 1980–2010 [8]. In the last decade, the only two inventories available are from 2016/2017 [15] and 2020 [16] with remarkable differences in the principles used to outline glaciers. These observational gaps and inconsistencies make tracking the changing glacier area in a timely and accurate manner challenging.

Synthetic Aperture Radar (SAR) technology, particularly through the Sentinel-1 mission, has the potential to greatly improve our ability to generate regular glacier inventories by offering consistent and high-temporal-resolution data regardless of weather conditions or daylight availability. This enhanced temporal resolution is particularly valuable for constraining physical models of glacier evolution, especially when studying rapidly changing phenomena such as calving fronts [17] and glacial surges, thus, leading to new insights into glacier dynamics.

Interferometric SAR (InSAR) coherence is generally recognised as a strong predictor for glacier outlines, especially for debris-covered tongues [18, 19]. Furthermore, SAR backscatter drops significantly during the melting season due to increased absorption of the radar signal by liquid water and reduced volumetric scaterring [20]. This temporal signal has been widely adopted to identify and

monitor glacier surface types [21, 22]. Despite its potential, the applicability of SAR time series to automate glacier outline mapping remains largely underexplored.

In this study, we introduce Intensity-Coherence-Evolution-mapper (ICEmapper), a deep learning model designed to map glacier outlines annually from Sentinel-1 time series. We systematically quantify uncertainties for both pixel-level predictions and overall area estimates—an aspect that has rarely been addressed comprehensively in deep-learning-based remote sensing and in previous glacier mapping efforts. We train ICEmapper using the 2016/2017 [15] and 2020 [16] glacier inventories. We apply this model to derive annual glacier outlines for the period 2016–2024 across Svalbard and analyse the glacier area changes. Our results show the increased response of glacier area to climate change in Svalbard and demonstrate the potential of our approach for tracking glacier changes, offering new perspectives on the dynamics of glacial ice loss.

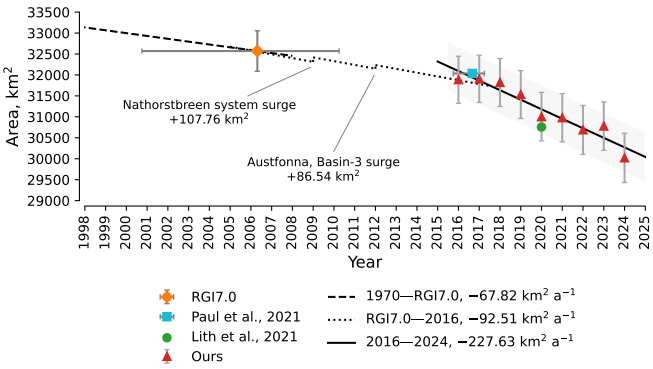

Fig. 1 Total glacier area change in Svalbard, except Kvitøya. Glaciers $< 2\,\mathrm{km}^2$ are excluded. Large glacier surges are shown schematically. X-error bands indicate minimum and maximum years for inventories derived from multi-year imagery, and y-error bands stand for the 95%-confidence interval for the total area (see Methods for details). For the evaluation of the 1970–RGI7.0 rate, see Supplementary Notes.

Results

Glacier area change analysis. To contextualise the results, we defined three distinct epochs of area change: (1) 1970–RGI7.0 compares historical glacier records from 1970s [23] with Randolph Glacier Inventory 7.0 (RGI7.0) [24], (2) RGI7.0–2016 compares the RGI7.0 outlines with our 2016 inventory, and (3) 2016–2024 analyses the annual inventories derived from ICEmapper. For all analyses below, we consider only polygons larger than $2\,\mathrm{km}^2$ as smaller glaciers are associated with higher mapping errors and interpretation uncertainties, in line with the protocol used by Nuth et al. (2013) [8] when comparing individual glacier outlines. Figure 1 shows the total glacier area evolution over the whole of Svalbard except Kvitøya, an island in the northeast part of the archipelago. Throughout the manuscript, uncertainties are expressed as 95% confidence intervals (95%-CI). For normally distributed variables we report $\pm 1.96\sigma$, whereas for the rest we provide the 2.5^{th}–97.5^{th} percentile range.

In the 1970–RGI7.0 epoch, we reevaluated the long-term trend because the figure of about $-80\,\mathrm{km}^2\,\mathrm{a}^{-1}$ from Nuth et al. (2013) [8] is a single point estimate without a formal error budget and therefore serves as a coarse baseline for judging modern glacier area loss acceleration rate. For this reevaluation, we implemented a resampling procedure that propagates the mapping error and the uncertainty of assigning one representative year to complete multi-year inventories, and that captures interannual variability in glacier area that occur during the inventory time spans (see Supplementary Notes). The revision shows a net loss of $-2481.50\,\mathrm{km}^2$, equivalent to $-68\,\mathrm{km}^2\,\mathrm{a}^{-1}$ (95%-CI $= -93.57$ to $-44.94\,\mathrm{km}^2\,\mathrm{a}^{-1}$) during 1970–RGI7.0.

During the RGI7.0–2016 epoch, the glacier area declined by $-702.14\,\mathrm{km}^2$ in total at a rate of $-72.46\,\mathrm{km}^2\,\mathrm{a}^{-1}$ (95%-CI $= -162.72$ to $+9.36\,\mathrm{km}^2\,\mathrm{a}^{-1}$, evaluated as for the previous epoch), which is not significantly different from zero. Notably, two large surges—the Nathorstbreen system ($+107.76\,\mathrm{km}^2$) started in 2009 [25] and Austfonna, Basin-3 ($+86.54\,\mathrm{km}^2$) in 2012 [26]—temporarily offset the region-wide glacier area loss. Their combined effect ($+194.30\,\mathrm{km}^2$ or $+0.60\%$) is estimated to have delayed net area shrinkage by a couple of years during the RGI7.0–2016 epoch. Subtracting the significant area gains of the advances of Nathorstbreen and Basin-3 from the trend of the RGI7.0–2016 epoch shows a more representative regionwide trend of $-92.51\,\mathrm{km}^2\,\mathrm{a}^{-1}$. Other parts of the archipelago show both positive (e.g., the northern part of Austfonna and the northeast of Spitsbergen) and negative (Edgeøya and the northwest of Spitsbergen) glacier area change trends (Figure 2a).

The annual inventories from ICEmapper between 2016–2024 reveal a sharply accelerated loss of glacier area of $-1821.02\,\mathrm{km}^2$ at a rate of $-227 \pm 75\,\mathrm{km}^2\,\mathrm{a}^{-1}$ (or $-0.71 \pm 0.23\%\,\mathrm{a}^{-1}$) throughout the archipelago. The net retreat is widespread (Figure 2b), with one considerable positive anomaly observed in Austfonna, Basin-7. This localised area increase stems from a surge event initiated around 2018/2019 (see Supplementary Notes).

We separately mapped Kvitøya using optical satellite imagery and GlaViTU [28], an existing glacier mapping model. The island was not included in the SAR-based inventories due to its coverage by a different radar imaging mode with a lower spatial resolution (see the Methods section for more detail). The glacier area change trend of Kvitøya from 2016 to 2024 is $-2.58\,\mathrm{km}^2\,\mathrm{a}^{-1}$ (or $-0.42\%\,\mathrm{a}^{-1}$), notably lower than the relative archipelago-wide rate reported above likely due to its location further north, yet still indicating a persistently negative trend. By 2024 glaciers occupy 52% of the land area of Svalbard, including glaciers $< 2\,\mathrm{km}^2$ and Kvitøya.

Because detailed, georeferenced outlines exist for both RGI7.0 and the ICEmapper inventories, we partition area change by glacier types for the RGI7.0–2016 and 2016–2024 epochs. Differentiating between tidewater and land-terminating glaciers reveals mixed results in the RGI7.0–2016 epoch: while their mean area change rates do not differ significantly (p-value > 0.05; compared using a two-sided Welch's t-test), the median rates do (p-value < 0.05; compared using a two-sided Mann-Whitney U test; Figure 3a). The same tests were used for comparing means

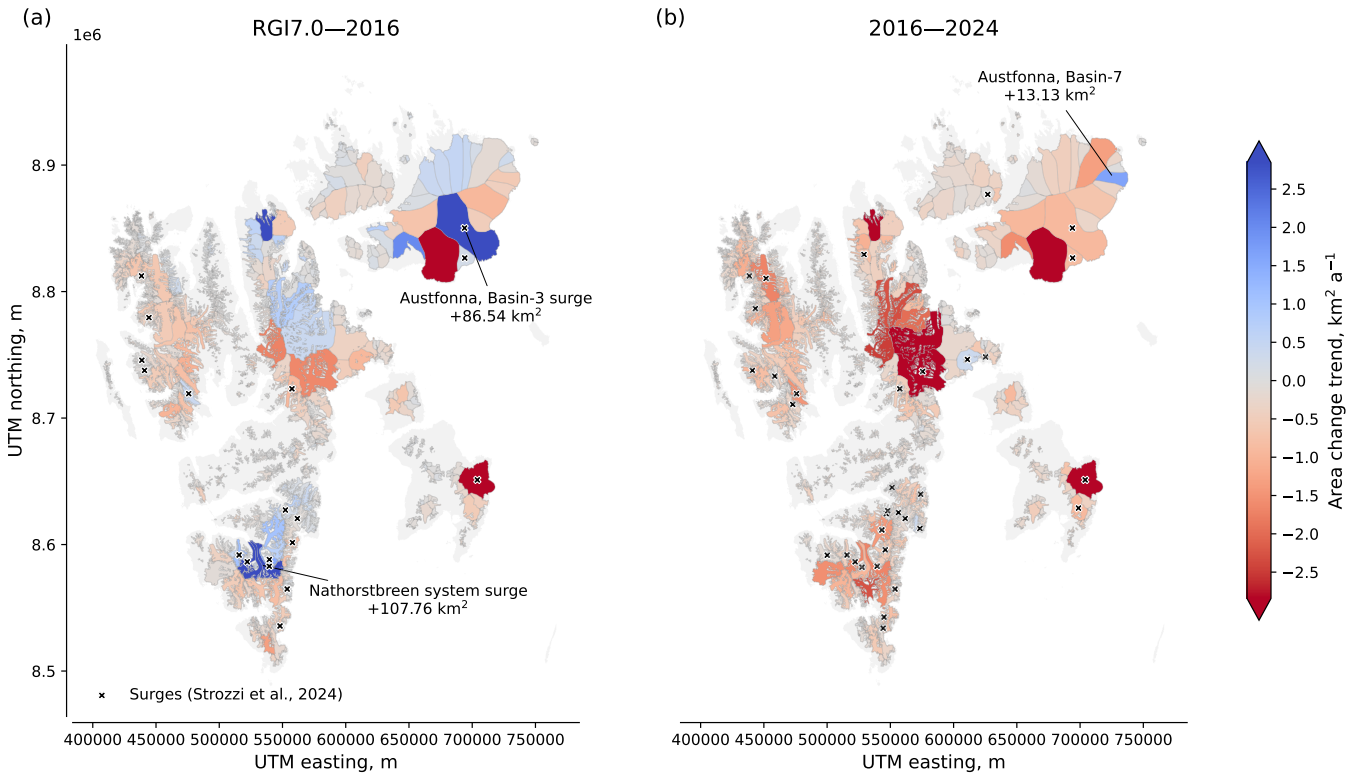

Fig. 2 Glacier area change trend maps: **a** for the RGI7.0–2016 epoch and **b** for the 2016–2024 epoch. The glacier outlines and ice divides are taken from Kohler et al., 2021 [16], and the glacier surge inventory is from Strozzi et al., 2024 [27].

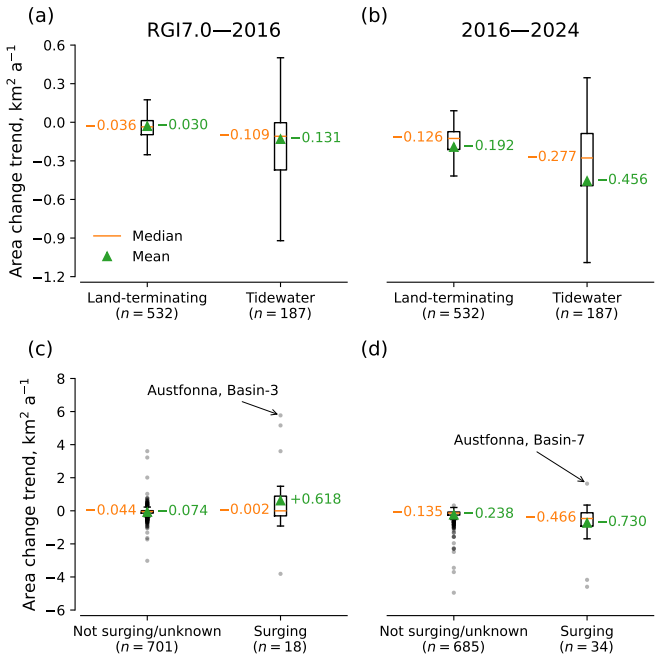

Fig. 3 Comparison of glacier area change trends: **a, b** for land-terminating vs tidewater and **c, d** for not surging vs surging glaciers **a, c** in the RGI7.0–2016 epoch and **b, d** in the 2016–2024 epoch. Only glaciers $> 2\,\mathrm{km}^2$ are used for comparison.

and medians throughout the manuscript. In contrast, the 2016–2024 epoch exhibits statistically significant distinctions in both means and medians, with tidewater glaciers undergoing a more pronounced retreat on average (Figure 3b). Both tidewater and land-terminating glaciers show statistically significant acceleration in their area loss (p-value < 0.05) when comparing RGI7.0–2016 to 2016–2024. Removing the known surging glaciers makes the means significantly different in RGI7.0–2016 as well, while all other conclusions remain unchanged. In total, tidewater glaciers contributed $-233.75\,\mathrm{km}^2$ (or 33.29%) to the overall glacier area loss in the RGI7.0–2016 epoch, and $-682.52\,\mathrm{km}^2$ (37.48%) of area loss in the 2016–2024 epoch.

For land-terminating glaciers in the RGI7.0–2016 epoch, there is a modest but statistically significant correlation ($r_s = 0.30$, p-value < 0.05; Supplementary Figure 3a) between area change rates and climatic mass-balance values modelled for the same period [29]. In the case of tidewater glaciers, no significant correlation was identified ($r_s = 0.14$, p-value ≈ 0.05; Supplementary Figure 3b), suggesting that processes at the ice-ocean interface play a dominant role in determining frontal ablation rates.

No significant difference in area change trends emerges between known surging [27] and non-surging glaciers in the RGI7.0–2016 epoch (p-value > 0.05; Figure 3c). In the 2016–2024 epoch, however, the area loss rates among surging glaciers are significantly higher (p-value < 0.05 for both means and medians; Figure 3d) compared to their non-surging counterparts, implying more rapid retreat on average. These conclusions remain the same in both epochs when restricting the analysis to surging tidewater glaciers alone. This contrast is apparent even though individual surges can cause short-term area gains.

ICEmapper performance. Given the nine-year analysis span and the comparably limited area change observed, it is crucial to ensure that our model meets ac-

Table 1 Test performance of ICEmapper. The reported metrics are defined in Methods, Accuracy Assessment.

Year	Number of test tiles	Pixel-wise IoU	Precision	Recall	Distance deviation, m			Total area deviation	
					Mean	Median	95$^{\text{th}}$ percentile	km^2	%
2016	34	0.992	0.996	0.996	34.17	0	118.75	+0.47	+0.02
2017	143	0.951	0.977	0.972	57.35	15.53	202.83	−25.33	−0.46
2020	179	0.965	0.982	0.982	63.28	14.42	207.78	+0.47	+0.01
Total	356	0.964	0.982	0.981	58.68	13.41	198.12	−24.39	−0.16

curacy requirements. The derived glacier outlines exhibit accuracy equivalent to human experts when delineating glaciers from optical images [30–32], with intersection over union (IoU) score higher than 0.95, total area discrepancies below 0.5%, a median distance deviation of approximately 15 m (or 1.5 pixel) and the 95$^{\text{th}}$ percentile distance deviation under 250 m (Table 1), affirming its effectiveness for glacier monitoring. Qualitative assessments also show good correspondence between the reference inventories and the modelled outlines, however, the performance over small glaciers, tributaries and some erratic debris-covered tongues remains inconsistent (Supplementary Figure 5). On the other hand, we like to highlight the IoU of 0.992, an almost 100% match between the reference and model outlines for the 2016 test subset covering two ice caps—Austfonna and Vestfonna (Table 1).

Additional, fully independent validation is provided in Supplementary Notes, where we benchmark ICEmapper-derived calving fronts against an expert-digitised inventory [33] and another deep-learning-based product [34]. In that analysis, our front position change rates agree with the expert data at $R^2 = 0.97$, and the mean (median) planimetric deviation is 58 m (35 m), which is about half of the error obtained for the outlines from [34].

Calibration of the modelled confidence against the actual accuracy yielded reliable per-pixel confidence estimates with expected calibration error below 0.5%, highlighting the areas prone to classification errors (Supplementary Figure 5). In particular, the pixel-level confidence maps allow confident detection of significant terminus shifts over the years, supporting spatio-temporal analyses of glacier front evolution (Supplementary Figure 6).

Discussion

Overall, our annual glacier inventories for Svalbard reveal a substantial acceleration of area loss since 2016. The conservative 2016–2024 glacier area change rate from our analysis is $-227 \pm 75\,\text{km}^2\,\text{a}^{-1}$, when limited to glaciers larger than $2\,\text{km}^2$. A consistent reevaluation of the 1970–2006 rate yields a historical baseline of $-68\,\text{km}^2\,\text{a}^{-1}$ (95%-CI = −93.57 to $-44.94\,\text{km}^2\,\text{a}^{-1}$; see Supplementary Notes), so the modern rate is 3.4 times higher and lies well outside the historical 95%-CI. Svalbard landmass area covered by glaciers has shrunk to 52% in 2024, versus 57% in the 2000s and 60% in the 1970s [8]. Extending the perspective further back to an existing 1936/1938 inventory [35] implies that overall retreat now proceeds at rates five to six times higher than the area change trend of approximately $-43\,\text{km}^2\,\text{a}^{-1}$ ($-0.13\%\,\text{a}^{-1}$) observed in the 1936/1938–RGI7.0 period, at least in the regions consistently covered in both the 1936/1938 inventory and RGI7.0, which are the whole of the archipelago except Kvitøya and some Eastern parts of Austfonna. Earlier inventories are separated by decades and provide only aggregate uncertainty estimates, if any. In contrast, the annual inventories presented here provide direct estimates of uncertainty at both pixel and archipelago scales, which enable a more robust assessment of modern glacier changes.

Looking to the future, negative mass balance projections for Svalbard[36] suggest that the glacier area will continue to decline. Even a halt in warming would not prevent further area loss due to the temporal lag between the climatic forcing and glacier geometry response [37] as most glaciers remain out of equilibrium with present climatic conditions. For tidewater glaciers in particular, declining seasonal sea ice duration [38] is likely to further exacerbate retreat as the presence of sea ice helps stabilise calving fronts [39–41]. Increased ocean heat content is expected to accelerate the area loss of tidewater glaciers as well [42].

Although both land-terminating and tidewater glacier types exhibit accelerating shrinkage, the 2016–2024 data indicate substantially higher retreat rates among tidewater glaciers, which are more sensitive to oceanic influences such as submarine melt and calving [42, 43]. In parallel, land-terminating glaciers display a measurable correlation with climatic mass balance, implying a primary driver related to atmospheric warming and, thus, surface melt. While the precise weighting of these processes remains an active research topic, the general message is that multiple climate forcings—both atmospheric and oceanic—contribute to the overall glacier recession ongoing in Svalbard. In total, while tidewater glaciers remain an important driver of the negative glacier area trend, land-terminating glaciers comprise a larger fraction of the overall area loss.

Turning to surging glaciers, large individual events can mask the underlying regional trend by imparting glacier area gains, thereby introducing non-linearity into the overall time series, as exemplified by Nathorstbreen and Austfonna, Basin-3. The analysis also shows that the average area change rates of the surging glaciers in 2016–2024 exceed those of non-surging glaciers. A plausible interpretation is that large individual surges, although adding glacier area temporarily, lead to a more pronounced retreat after the active surge phase ends, linked to thinning-induced dynamic instabilities and higher incidence of calving [26] due to, e.g., increased crevassing [44] and lateral wastage [8].

Moreover, the mass redistribution during surges typically lowers the elevation in the accumulation zone by tens of meters as well as effectively transport ice to the terminus area [40, 45], exposing both to warmer air and, thus, intensifying melt [46]. Further monitoring over extended periods is necessary to confirm whether the higher losses among surging glaciers reflect a consistent trend or whether it is partly coincidental within our relatively short observation window of a decade.

Additionally, we recognised an increasingly larger extent and surge-induced glacier area encroachment from adjacent flow units at the kilometre scale, while tracking the low coherence zone of, e.g., Austfonna, Basin-3 (Supplementary Figure 11). Because our inventories rely on static ice divides copied from the existing datasets, these surge-driven changes are not fully captured, highlighting the need for more frequent ice divide updates derived from velocity products that can better resolve glacier flow boundaries. Such refined delineations would also benefit ice cap-wide glacier evolution modelling.

While the overall accuracy of ICEmapper aligns closely with expert digitisation and demonstrates robust performance on most glacier margins, the model exhibits inconsistencies in mapping smaller ice masses and tributaries. These localised errors are likely driven by a combination of limited feature contrast of glaciers in SAR imagery and variations in how small glaciers were delineated across different reference inventories used for training, as the 2016/2017 inventory [15] tends to include smaller ice patches in general. Future work should test the transferability of ICEmapper to regions with higher debris cover and steeper terrain, as well as to other SAR platforms with longer revisit times and irregular acquisition schedules. Moreover, improvements could include utilising images from both ascending and descending passes, higher-resolution SAR data, more sophisticated data fusion methods that incorporate, e.g., optical or thermal imagery and the expansion of training sets to cover a broader diversity of glacier types and environmental conditions. Such expansions would facilitate a more globally consistent framework for glacier mapping and enable future applications of ICEmapper to other polar and high-mountain regions experiencing glacier retreat, fulfilling the GCOS standards for glacier area monitoring.

In summary, our annual glacier outlines indicate that Svalbard has entered a phase of accelerated glacier area loss in the last years, likely driven by the combined influences of warming atmospheric and ocean conditions. Despite certain limitations, such as reduced accuracy for smaller ice patches, the results demonstrate the utility of an automated deep learning method for generating high-temporal-resolution (i.e., annual) glacier inventories, enabling regionwide glacier area change analysis at decadal or shorter time scales. Continued monitoring in Svalbard and other regions at annual intervals will be essential to better understand processes that govern glacier recession, inform glacier evolution models and evaluate the impacts of cryospheric changes on sea-level contributions and polar environments.

Methods

Study area and data. Our study focused on Svalbard, utilising Sentinel-1A imagery to cover almost the entirety of the region, excluding Kvitøya. The satellite data included images from two ascending orbit stripes (relative orbits 14 and 174) acquired in the interferometric wide (IW) swath mode. To train our models, we used 30 co-polarised (HH) ground range detected (GRD) and radiometrically terrain corrected (RTC) [47] mosaics per year. These images were resampled to a spatial resolution of $10\,\mathrm{m} \times 10\,\mathrm{m}$ from the original resolution of $5\,\mathrm{m} \times 20\,\mathrm{m}$, with a 12-day interval between acquisitions. Additionally, we incorporated InSAR coherence imagery into our analysis computed at the 12-day temporal baseline.

For reference data in training and evaluation, we utilised two glacier inventories from the years 2016/2017 [15] and 2020 [16] (a preliminary version, kindly provided by the authors). The 2016/2017 inventory was spatially and temporally uncoupled, meaning that images from 2016 and 2017 were used distinctly according to their corresponding outlines.

Although the 2016/2017 inventory remains unpublished and the 2020 inventory is a preliminary release, both are of mapping quality comparable to other expert-digitised glacier datasets. Residual issues—e.g. mislabelled snow patches, tiny isolated polygons or small tributaries—do not affect the actual glacier outlines considerably. In practice, such label noise acts as a regulariser for deep learning models and can improve generalisation [48], while providing a realistic basis for uncertainty quantification, i.e., better depicting the inconsistencies in existing glacier inventories. We therefore consider these two inventories fully adequate for training and evaluating ICEmapper.

The whole geographical domain was divided into 734 square tiles, each measuring 10 km by 10 km. We randomly allocated 60% of the tiles to use for training, 20% for validation, and the remaining 20% for testing. Tiles that did not cover glacierised landmass were excluded from the training dataset, as well as Kvitøya island due to its coverage by Sentinel-1 in a different imaging mode with a lower spatial resolution as compared to the rest of the archipelago. For generating the final glacier inventories, we utilised 15 scenes per year with a 24-day gap between acquisitions. The temporal baselines for the InSAR coherence images were maintained at 12 days for all years, except 2024 where the 24-day baseline provided qualitatively better outcomes. An overview of the study area is provided in Supplementary Figure 4.

ICEmapper. We refined our previous glacier mapping method [49] by introducing a revised model called Intensity-Coherence-Evolution-mapper (ICEmapper, Supplementary Figure 7), which transforms a one-year time series of SAR images into glacier outlines as they are observed at the end of the ablation season. ICEmapper is based on the U-Net architecture [50] and incorporates 3D convolutions in the decoder part to process temporal and spatial dimensions simultaneously similar to other studies [51].

Patches of 384×384 pixels were extracted randomly for model training. From the 30 available timesteps per year, 15 were sampled for training, each spaced by a 24-day gap. To further enhance the robustness to temporal variations, we introduced random noise of ± 12 days for individual timesteps to the sampling as part of the data augmentation process. Additionally, data augmentation included random flipping, rotation, cropping, rescaling, contrast γ-transformation and Gaussian noise introduction. The optimisation was performed using Adam [52] minimising focal loss [53] with the addition of label smoothing [54]. We employed a cosine annealing schedule with warm restarts for the learning rate [55], initiating at $5e^{-4}$ and progressing through four training phases of 10, 20, 40, and 80 epochs. Selection for further evaluation was restricted to models demonstrating the highest performance on the validation subset.

Compared to our previous study [49], we replaced the max pooling layers with time-weighted pooling (Supplementary Figure 8) to allow for more adaptive extraction of the temporal features. The time-weighted pooling effectively computes a weighted average of the hidden representations along the temporal dimension, where the weights are calculated from the data itself. The time-weighted pooling showed marginal validation performance gains (Supplementary Table 3) and demonstrated better convergence properties (Supplementary Figure 9), hence, we used the time-weighted pooling layers in the rest of the experiments.

We explored various feature sets including GRD, RTC and InSAR coherence data, as well as combinations of GRD and RTC with InSAR. Our results indicate that the combination of GRD and InSAR achieves the best overall validation performance (Supplementary Table 3), though the performance gap from RTC and InSAR was rather minor. Given the additional processing step for the generation of RTC imagery, the GRD and InSAR combination provides a more computationally efficient alternative as well. We, thus, used GRD and InSAR to report the test performance and produce the final glacier inventories. The test performance of ICEmapper aligns with the expertise level of human analysts [30–32] with the total area difference $< 0.5\%$, median distance deviation $\approx 15\,\mathrm{m}$ and the 95^{th} distance deviation percentile $< 250\,\mathrm{m}$ (Table 1).

Postprocessing. We implemented several procedures to eliminate some spurious predictions. We removed all polygons smaller than $0.01\,\mathrm{km}^2$ following a common practice in glacier inventory generation [56]. We also excluded any positive predictions that extended beyond the boundaries of a 3840 m buffer, which was established based on the union of known glacier inventories including RGI7.0 [24] and the inventories used in this study [15, 16]. This buffer served as a spatial constraint to refine our analysis to areas with confirmed glacier presence.

An additional temporal filtering was applied to the pixel-level predictions. If a pixel was classified as a glacier in a given year t_i but was predicted with high confidence ($> 90\%$) as non-glacier in adjacent years t_{i-1} and t_{i+1}, the classification for the year t_i was revised to non-glacier. This correction was also applied in reverse—if a pixel was classified as non-glacier at t_i yet identified as glacier with high confidence in t_{i-1} and t_{i+1}, it was reclassified as glacier for the year t_i.

As the pixel-level temporal filtering cannot be applied to years 2016 and 2024, as a similar measure we removed all isolated polygons $> 1\,\mathrm{km}^2$ that do not have intersections with any polygon from the adjacent years in the predictions, assuming that large ice complexes do not appear and disappear suddenly. These measures ensured overall higher temporal consistency of the generated inventories.

Uncertainty quantification. We used plain softmax scores from a single forward pass to assess classification confidence, similar to our other work [28]. We employed a Shannon-entropy-based metric to measure confidence:

$$\mathrm{conf}\,(S_i) = 1 + (1 - S_i)\,\log_2\,(1 - S_i) + S_i \log_2 S_i\,, \qquad (1)$$

where S_i is the softmax score attributed to the glacier class at the i^{th} pixel, and $\log_2\,(\cdot)$ denotes the logarithm base 2. Initially, these scores exhibited high underconfidence. To enhance the reliability of our uncertainty estimates, we implemented a confidence calibration approach through kernel ridge regression aimed at aligning the predicted confidence levels with actual model accuracy. This calibration significantly reduced the expected calibration error to $< 0.5\%$ (Supplementary Figure 10) allowing for tracking significant changes in glacier terminus positions at the pixel level (Supplementary Figure 6).

The total area uncertainty was estimated with block bootstrapping [57]. The area estimator is:

$$A^* = a \cdot \sum_{i=1}^{n} p\,(T_i = 1)\,, \qquad (2)$$

where a is the area of one pixel, n is the total number of pixels, and $p\,(T_i = 1)$ is the probability of the i^{th} pixel being a glacier defined as:

$$p\,(T_i = 1) = \begin{cases} C_i & \text{if } L_i = 1 \\ 1 - C_i & \text{else} \end{cases}\,, \qquad (3)$$

with C_i and L_i being, respectively, the calibrated confidence and the model label assigned to the i^{th} pixel. We partitioned the entire archipelago into non-overlapping square windows of side length b (selected via the optimisation procedure described below). We then drew random resamples with replacement of these windows and calculated the corresponding area values, A^*. This process was repeated 10 000 times, and the corresponding area uncertainty bands were calculated as the 2.5^{th} and 97.5^{th} percentiles of the bootstrapping distribution of A^*.

The optimal window size b for block bootstrapping was estimated by minimising the mean squared error between bootstrapped distributions and known areas from the 2016/2017 [15] and 2020 [16] inventories:

$$\mathrm{E}\left[(A_b^* - A)^2\right] = \mathrm{Var}\,[A_b^*] + (\mathrm{E}\,[A_b^*] - A)^2 \to \min_b\,, \qquad (4)$$

where A are the known total area values. We assumed insignificant total area change between 2016 and 2017, considering that only a single multi-year inventory covers both years and our results show a small area change between 2016 and 2017. Among three window sizes optimised independently for all three years, we chose the maximum one, noted for providing the highest variance, $b = 3.2\,\mathrm{km}$ in 2020, resulting in a total sample of 5 330 windows. This window size was then applied to the remaining years for the final inference. Lastly, we recentred the bootstrapping distributions so their means match the vectorised outputs of the model, ensuring consistency between the reported figures and the generated inventories.

Kvitøya outlines. For completeness, we mapped Kvitøya from 2016 to 2024 using GlaViTU [28] and optical imagery, and published it together with the glacier inventories for the rest of the archipelago. We utilised Landsat 8 and 9 images that are suitable for glacier mapping, i.e. acquired close to the end of the ablation season with minimal cloud coverage and absence of sea ice. Successfully, we derived the outlines of Kvitøya for 2016, 2018, 2020, 2022, 2023 and 2024.

Accuracy assessment. The classification performance was evaluated using intersection over union (IoU), precision and recall, defined by:

$$\mathrm{IoU} = |\,T \cap P\,|\,/\,|\,T \cup P\,|\,, \qquad (5)$$

$$\mathrm{Precision} = |\,T \cap P\,|\,/\,|\,P\,|\,, \qquad (6)$$

$$\mathrm{Recall} = |\,T \cap P\,|\,/\,|\,T\,|\,, \qquad (7)$$

where T and P denote the reference and predicted glacier pixels, respectively.

The differences in glacierised area were assessed using both absolute and relative metrics:

$$\Delta A = A_{\mathrm{pred}} - A_{\mathrm{ref}}\,, \quad \delta A = (A_{\mathrm{pred}} - A_{\mathrm{ref}})\,/A_{\mathrm{ref}}\,, \qquad (8)$$

where A_{pred} is the predicted glacierised area, and A_{ref} is the reference area.

Distance deviations between the predicted and reference glacier boundaries were calculated using a PoLiS-like met-

ric [58], which considers the average distances between boundary points:

$$\overline{\rho(\text{pred},\text{ref})} = \frac{1}{|\{p\in\text{pred}\cup\text{ref}\}|}\left(\sum_{\{p\in\text{pred}\}}\rho\,(p,\text{ref}) + \sum_{\{p\in\text{ref}\}}\rho\,(p,\text{pred})\right), \quad (9)$$

where p stands for the boundary points, ref and pred are the reference and predicted boundaries, respectively, and ρ is the Euclidean distance. Points were sampled every 10 m along all boundaries within a tile to derive this metric. Additional statistics—median and the 95$^{\text{th}}$ percentile—were provided to offer a more detailed view of the variation in distance deviations.

Computational resources. We trained and deployed the models on a cloud server equipped with an NVIDIA RTX A6000 GPU, a 128-core 2.5 GHz CPU and 1 TB RAM. The training duration for one model ranged from three to four days, depending on the number of input features. Applying the model to the complete dataset spanning 2016 to 2024 took a day.

Data availability

The datasets generated during and/or analysed during the current study will be available upon publication.

Code availability

Our codebase and the pretrained models will be available upon publication.

References

1. Hock, R. *et al.* High Mountain Areas. *IPCC Special Report on the Ocean and Cryosphere in a Changing Climate* (eds Pörtner, H.-O. *et al.*) 131–202. https://www.ipcc.ch/srocc/chapter/chapter-2/ (2019).
2. Meredith, M. *et al.* Polar Regions. *IPCC Special Report on the Ocean and Cryosphere in a Changing Climate* (eds Pörtner, H.-O. *et al.*) 203–320. https://www.ipcc.ch/srocc/chapter/chapter-3-2/ (2019).
3. Zemp, M. *et al.* Global glacier mass changes and their contributions to sea-level rise from 1961 to 2016. *Nature* **568,** 382–386. ISSN: 14764687 (7752 Apr. 2019).
4. Hugonnet, R. *et al.* Accelerated global glacier mass loss in the early twenty-first century. *Nature* **592,** 726–731. ISSN: 14764687 (7856 Apr. 2021).
5. Rounce, D. R. *et al.* Global glacier change in the 21st century: Every increase in temperature matters. *Science* **379,** 78–83. ISSN: 10959203. https://www.science.org/doi/10.1126/science.abo1324 (6627 Jan. 2023).
6. Rantanen, M. *et al.* The Arctic has warmed nearly four times faster than the globe since 1979. *Nature Communications Earth & Environment* **3.** ISSN: 2662-4435. https://www.nature.com/articles/s43247-022-00498-3 (1 Aug. 2022).
7. Osuch, M. & Wawrzyniak, T. Inter- and intra-annual changes in air temperature and precipitation in western Spitsbergen. *International Journal of Climatology* **37,** 3082–3097. eprint: https://rmets.onlinelibrary.wiley.com/doi/pdf/10.1002/joc.4901. https://rmets.onlinelibrary.wiley.com/doi/abs/10.1002/joc.4901 (2017).
8. Nuth, C. *et al.* Decadal changes from a multi-temporal glacier inventory of Svalbard. *The Cryosphere* **7,** 1603–1621. https://tc.copernicus.org/articles/7/1603/2013/ (2013).
9. Spolaor, A. *et al.* Climate change is rapidly deteriorating the climatic signal in Svalbard glaciers. *The Cryosphere* **18,** 307–320. https://tc.copernicus.org/articles/18/307/2024/ (2024).
10. Łupikasza, E. B. *et al.* The Role of Winter Rain in the Glacial System on Svalbard. *Water* **11.** ISSN: 2073-4441. https://www.mdpi.com/2073-4441/11/2/334 (2019).
11. Schuler, T. V. *et al.* Reconciling Svalbard Glacier Mass Balance. *Frontiers in Earth Science* **8.** ISSN: 2296-6463. https://www.frontiersin.org/journals/earth-science/articles/10.3389/feart.2020.00156 (2020).
12. Ingrosso, G. *et al.* Greening of Svalbard in the twentieth century driven by sea ice loss and glaciers retreat. *Communications Earth & Environment* **6,** 30. ISSN: 2662-4435. https://doi.org/10.1038/s43247-025-01994-y (Jan. 2025).
13. World Meteorological Organization, United Nations Environment Programme, International Science Council & Intergovernmental Oceanographic Commission of the United Nations Educational, Scientific and Cultural Organization. *The 2022 GCOS ECVs Requirements (GCOS 245)* 2022. https://library.wmo.int/idurl/4/58111.
14. Racoviteanu, A. E., Paul, F., Raup, B., Khalsa, S. J. S. & Armstrong, R. Challenges and recommendations in mapping of glacier parameters from space: results of the 2008 Global Land Ice Measurements from Space (GLIMS) workshop, Boulder, Colorado, USA. *Annals of Glaciology* **50,** 53–69. ISSN: 0260-3055 (53 2009).
15. Paul, F., Goerlich, F. & Rastner, P. *A new glacier inventory for Svalbard from Sentinel-2 and Landsat 8 for improved calculation of climate change impacts* in *EGU General Assembly* (2021, online, 19–30 Apr 2021, EGU21-14499). https://doi.org/10.5194/egusphere-egu21-14499.
16. Kohler, J., Lith, A. & Moholdt, G. *Svalbard glacier inventory based on Sentinel-2 imagery from summer 2020* 2021. https://doi.org/10.21334/npolar.2021.1b8631bf.
17. Muñoz-Hermosilla, J. M. *et al.* A 3D glacier dynamics–line plume model to estimate the frontal ablation of Hansbreen, Svalbard. *The Cryosphere* **18,** 1911–1924. https://tc.copernicus.org/articles/18/1911/2024/ (2024).
18. D. K. Atwood, F. M. & Arendt, A. Using L-band SAR coherence to delineate glacier extent. *Canadian Journal of Remote Sensing* **36,** S186–S195. eprint: https://doi.org/10.5589/m10-014. https://doi.org/10.5589/m10-014 (2010).
19. Lippl, S., Vijay, S. & Braun, M. Automatic delineation of debris-covered glaciers using InSAR coherence derived from X-, C- and L-band radar data: a case study of Yazgyl Glacier. *Journal of Glaciology* **64,** 811–821 (2018).

20. Hallikainen, M., Ulaby, F. & Abdelrazik, M. Dielectric properties of snow in the 3 to 37 GHz range. *IEEE Transactions on Antennas and Propagation* **34,** 1329–1340 (1986).

21. Winsvold, S. H. *et al.* Using SAR satellite data time series for regional glacier mapping. *The Cryosphere* **12,** 867–890. https://tc.copernicus.org/articles/12/867/2018/ (2018).

22. Barzycka, B., Błaszczyk, M., Grabiec, M. & Jania, J. Glacier facies of Vestfonna (Svalbard) based on SAR images and GPR measurements. *Remote Sensing of Environment* **221,** 373–385. ISSN: 0034-4257. https://www.sciencedirect.com/science/article/pii/S0034425718305297 (2019).

23. World Glacier Monitoring Service. *World Glacier Inventory, Version 1* https://doi.org/10.7265/N5/NSIDC-WGI-2012-02.

24. RGI Consortium. Randolph Glacier Inventory—A Dataset of Global Glacier Outlines, Version 7. *Boulder, Colorado USA. NSIDC: National Snow and Ice Data Center.* (2023).

25. Nuth, C. *et al.* Dynamic vulnerability revealed in the collapse of an Arctic tidewater glacier. *Scientific Reports* **9,** 5541. ISSN: 2045-2322. https://doi.org/10.1038/s41598-019-41117-0 (Apr. 2019).

26. Dunse, T. *et al.* Glacier-surge mechanisms promoted by a hydro-thermodynamic feedback to summer melt. *The Cryosphere* **9,** 197–215. https://tc.copernicus.org/articles/9/197/2015/ (2015).

27. Strozzi, T., Cantus, O. & Santoro, M. *Glaciers_CCI project: ERS-1/2 C-band data over Svalbard* Project Report (GAMMA Remote Sensing AG, Switzerland, Oct. 2024).

28. Maslov, K. A., Persello, C., Schellenberger, T. & Stein, A. Globally scalable glacier mapping by deep learning matches expert delineation accuracy. *Nature Communications* **16,** 43. ISSN: 2041-1723. https://doi.org/10.1038/s41467-024-54956-x (2025).

29. Van Pelt, W. *et al.* A long-term dataset of climatic mass balance, snow conditions, and runoff in Svalbard (1957–2018). *The Cryosphere* **13,** 2259–2280. https://tc.copernicus.org/articles/13/2259/2019/ (2019).

30. Paul, F. *et al.* On the accuracy of glacier outlines derived from remote-sensing data. *Annals of Glaciology* **54,** 171–182. ISSN: 02603055 (July 2013).

31. Raup, B. H. *et al.* Quality in the GLIMS Glacier Database. *Global Land Ice Measurements from Space,* 163–182. https://link.springer.com/chapter/10.1007/978-3-540-79818-7_7 (2014).

32. Linsbauer, A. *et al.* The New Swiss Glacier Inventory SGI2016: From a Topographical to a Glaciological Dataset. *Frontiers in Earth Science* **9,** 704189. ISSN: 22966463 (Oct. 2021).

33. Moholdt, G., Maton, J., Majerska, M. & Kohler, J. *Annual frontlines of marine-terminating glaciers on Svalbard* 2021. https://data.npolar.no/dataset/d60a919a-9cc8-4048-9686-df81bfdc2338.

34. Li, T. *et al.* A high-resolution calving front data product for marine-terminating glaciers in Svalbard. *Earth System Science Data* **16,** 919–939. https://essd.copernicus.org/articles/16/919/2024/ (2024).

35. Geyman, E., van Pelt, W., Maloof, A., Aas, H. & Kohler, J. *1936/1938 DEM of Svalbard* 2021. https://doi.org/10.21334/npolar.2021.f6afca5c.

36. Geyman, E. C., J. J. van Pelt, W., Maloof, A. C., Aas, H. F. & Kohler, J. Historical glacier change on Svalbard predicts doubling of mass loss by 2100. *Nature* **601,** 374–379. ISSN: 1476-4687. https://doi.org/10.1038/s41586-021-04314-4 (Jan. 2022).

37. Zekollari, H., Huss, M. & Farinotti, D. On the Imbalance and Response Time of Glaciers in the European Alps. *Geophysical Research Letters* **47.** e2019GL085578 2019GL085578, e2019GL085578. eprint: https://agupubs.onlinelibrary.wiley.com/doi/pdf/10.1029/2019GL085578. https://agupubs.onlinelibrary.wiley.com/doi/abs/10.1029/2019GL085578 (2020).

38. Urbański, J. A. & Litwicka, D. The decline of Svalbard land-fast sea ice extent as a result of climate change. *Oceanologia* **64,** 535–545. ISSN: 0078-3234. https://www.sciencedirect.com/science/article/pii/S0078323422000495 (2022).

39. Krug, J., Durand, G., Gagliardini, O. & Weiss, J. Modelling the impact of submarine frontal melting and ice mélange on glacier dynamics. *The Cryosphere* **9,** 989–1003. https://tc.copernicus.org/articles/9/989/2015/ (2015).

40. Morris, A., Moholdt, G. & Gray, L. Spread of Svalbard Glacier Mass Loss to Barents Sea Margins Revealed by CryoSat-2. *Journal of Geophysical Research: Earth Surface* **125.** e2019JF005357 10.1029/2019JF005357, e2019JF005357. eprint: https://agupubs.onlinelibrary.wiley.com/doi/pdf/10.1029/2019JF005357. https://agupubs.onlinelibrary.wiley.com/doi/abs/10.1029/2019JF005357 (2020).

41. Tepes, P. *et al.* Changes in elevation and mass of Arctic glaciers and ice caps, 2010–2017. *Remote Sensing of Environment* **261,** 112481. ISSN: 0034-4257. https://www.sciencedirect.com/science/article/pii/S0034425721001991 (2021).

42. Li, T. *et al.* Pervasive glacier retreats across Svalbard from 1985 to 2023. *Nature Communications* **16,** 705. ISSN: 2041-1723. https://doi.org/10.1038/s41467-025-55948-1 (Jan. 2025).

43. Wood, M. *et al.* Ocean-Induced Melt Triggers Glacier Retreat in Northwest Greenland. *Geophysical Research Letters* **45,** 8334–8342. eprint: https://agupubs.onlinelibrary.wiley.com/doi/pdf/10.1029/2018GL078024. https://agupubs.onlinelibrary.wiley.com/doi/abs/10.1029/2018GL078024 (2018).

44. Leclercq, P. W., Kääb, A. & Altena, B. Brief communication: Detection of glacier surge activity using cloud computing of Sentinel-1 radar data. *The Cryosphere* **15,** 4901–4907. https://tc.copernicus.org/articles/15/4901/2021/ (2021).

45. Beraud, L., Brun, F., Dehecq, A., Hugonnet, R. & Shekhar, P. Glacier surge monitoring from temporally dense elevation time series: application to an ASTER dataset over the Karakoram region. *EGUsphere* **2024,** 1–32. https://egusphere.copernicus.org/preprints/2024/egusphere-2024-3480/ (2024).

46. Guillet, G. *et al.* A regionally resolved inventory of High Mountain Asia surge-type glaciers, derived from a multi-factor remote sensing approach. *The Cryosphere* **16,** 603–623. https://tc.copernicus.org/articles/16/603/2022/ (2022).

47. Frey, O., Santoro, M., Werner, C. L. & Wegmuller, U. DEM-Based SAR Pixel-Area Estimation for Enhanced Geocoding Refinement and Radiometric Normalization. *IEEE Geoscience and Remote Sensing Letters* **10,** 48–52 (2013).

48. Xie, L., Wang, J., Wei, Z., Wang, M. & Tian, Q. *DisturbLabel: Regularizing CNN on the Loss Layer* in *2016 IEEE Conference on Computer Vision and Pattern Recognition (CVPR)* (2016), 4753–4762.

49. Maslov, K. A., Schellenberger, T., Persello, C. & Stein, A. *Glacier Mapping from Sentinel-1 SAR Time Series with Deep Learning in Svalbard* in *IGARSS 2024 - 2024 IEEE International Geoscience and Remote Sensing Symposium* (2024), 14–17.

50. Ronneberger, O., Fischer, P. & Brox, T. U-Net: Convolutional Networks for Biomedical Image Segmentation. *Lecture Notes in Computer Science (including subseries Lecture Notes in Artificial Intelligence and Lecture Notes in Bioinformatics)* **9351,** 234–241. ISSN: 16113349. https://arxiv.org/abs/1505.04597v1 (May 2015).

51. Tran, D., Bourdev, L., Fergus, R., Torresani, L. & Paluri, M. *Learning Spatiotemporal Features With 3D Convolutional Networks* in *Proceedings of the IEEE International Conference on Computer Vision (ICCV)* (Dec. 2015).

52. Kingma, D. P. & Ba, J. L. *Adam: A Method for Stochastic Optimization* in *3rd International Conference on Learning Representations, ICLR 2015 - Conference Track Proceedings* (International Conference on Learning Representations, ICLR, Dec. 2014). https://arxiv.org/abs/1412.6980v9.

53. Lin, T.-Y., Goyal, P., Girshick, R., He, K. & Dollár, P. *Focal Loss for Dense Object Detection* in *2017 IEEE International Conference on Computer Vision (ICCV)* (2017), 2999–3007.

54. Müller, R., Kornblith, S. & Hinton, G. When Does Label Smoothing Help? *Advances in Neural Information Processing Systems* **32.** ISSN: 10495258. https://arxiv.org/abs/1906.02629v3 (June 2019).

55. Loshchilov, I. & Hutter, F. *SGDR: Stochastic Gradient Descent with Warm Restarts* in *5th International Conference on Learning Representations, ICLR 2017 - Conference Track Proceedings* (International Conference on Learning Representations, ICLR, Aug. 2016). https://arxiv.org/abs/1608.03983v5.

56. Paul, F. *et al.* Recommendations for the compilation of glacier inventory data from digital sources. *Annals of Glaciology* **50,** 119–126. ISSN: 0260-3055. https://www.cambridge.org/core/journals/annals-of-glaciology/article/recommendations-for-the-compilation-of-glacier-inventory-data-from-digital-sources/6BAE48BE4B8FEEEEBCFB59A2684A2427 (53 2009).

57. Hall, P., Horowitz, J. L. & Jing, B.-Y. On Blocking Rules for the Bootstrap with Dependent Data. *Biometrika* **82,** 561–574. ISSN: 00063444, 14643510. http://www.jstor.org/stable/2337534 (1995).

58. Avbelj, J., Müller, R. & Bamler, R. A Metric for Polygon Comparison and Building Extraction Evaluation. *IEEE Geoscience and Remote Sensing Letters* **12,** 170–174 (2015).

Acknowledgements

This research was financed by the Research Council of Norway under the "Researcher Project for Scientific Renewal" (project MASSIVE, no. 315971) awarded to T.S., C.P., A.S. and K.A.M. Additional support was provided by Open Clouds for Research Environments under the EU H2020 programme (project MATS_CLOUD, no. 824079) for access to the CREODIAS cloud platform for computing and seamless remote sensing data retrieval, awarded to C.P., T.S. and K.A.M.

We thank J. Kohler, A. Lith and G. Moholdt from the Norwegian Polar Institute for generously providing an early version of the 2020 Svalbard inventory used for model training and T. Strozzi from GAMMA Remote Sensing AG for generously providing the glacier surge inventory for Svalbard. We also kindly thank E. S. Mannerfelt from the University of Oslo for providing us with the updated dynamic basin boundaries of Austfonna, Basin-3 (Supplementary information).

Author contributions

T.S., K.A.M. and C.P. designed the study. K.A.M. implemented the methods and conducted the analysis. K.A.M., T.S., C.P. and A.S. discussed the results extensively. T.S. had the project idea and leads the project with C.P. K.A.M. wrote the manuscript. T.S., C.P. and A.S. reviewed the manuscript.

Competing interests

The authors declare no competing interests.

Supplementary information

Three times accelerated glacier area loss in Svalbard revealed by deep learning

Konstantin A. Maslov, Thomas Schellenberger, Claudio Persello, Alfred Stein

Supplementary Notes

Reevaluation of the historical glacier area change rate. Nuth et al. (2013) [1] reported the area change rate of $-80\,\mathrm{km}^2\,\mathrm{a}^{-1}$ for 1980–2010 in Svalbard. This estimation, however, relies on two glacier inventories—one by Hagen et al. (1993) [2] and an outdated version of RGI [1]—and lacks uncertainty estimates related to their multi-year nature, complicating comparison of our reported rates with this historical baseline. Here, we reevaluate the historical trend using two closest up-to-date proxies of the original data sources used by Nuth et al. (2013) [1] and report its uncertainty to make a more robust evaluation of the acceleration rate suggested by our results.

Hagen et al. (1993) [2] data are based on several aerial campaigns and are not available digitally. The closest proxy we could obtain is the World Glacier Inventory (WGI) [3]. It contains glacier areas, mapping years and approximate glacier locations, and is mostly based on revised Hagen et al. (1993) [2] data. For RGI, we used the latest available version, which is RGI7.0 [4]. Given that both datasets are updated or revised versions of those used by Nuth et al. (2013) [1], we at least do not degrade our historical trend reevaluation. We removed all glacier units $< 2\,\mathrm{km}^2$ from the analysis, as smaller glaciers are associated with higher mapping errors and might be confused with snowpacks. Kvitøya was also excluded.

For each inventory i, we have M_i pairs if t_{ij} and w_{ij}—the years of mapping and the portions of the total inventory area mapped in each year ($\sum_j w_{ij} = 1$)—as well as the total inventory areas S_i^{obs}. Nuth et al. (2013) [1] reported a "conservative uncertainty estimate" of $500\,\mathrm{km}^2$ for the total area of their mapping results, which we read as 1.96σ—consistent with the language they use ("95%-CI") when describing single glacier area uncertainties. We assume the same relative mapping uncertainty for WGI and RGI, as well as that these errors are independent. We also define the representative year of every inventory as its area-weighted average year, $T_i^{\mathrm{obs}} = \sum_j w_{ij} t_{ij}$. That gives us the temporal spread between the two inventories $T_2^{\mathrm{obs}} - T_1^{\mathrm{obs}} \approx 37$ years. Supplementary Table 1 summarises the historical inventory data.

We propose a straightforward resampling procedure to infer glacier area change rate from the two inventories and estimate its confidence interval. The procedure considers uncertanty in mapping and in assigning a representative year to a whole multi-year inventory as well as area changes that occured between the year of mapping of a particular portion of an inventory and the representative year. Let f denote the regionwide fractional area change rate. Then,

Supplementary Table 1 Historical inventory data.

WGI [3]		RGI [4]	
t_{1j}	w_{1j}, %	t_{2j}	w_{2j}, %
1960	3.75	2001	11.83
1961	10.47	2002	7.67
1966	19.26	2003	1.48
1969	16.44	2004	4.28
1970	18.46	2005	11.56
1971	8.96	2006	0.12
1977	12.57	2007	11.88
1980	10.08	2008	60.45
		2009	0.05
		2010	0.67
$S_1^{\mathrm{obs}} = 35039.93\,\mathrm{km}^2$		$S_2^{\mathrm{obs}} = 32570.49\,\mathrm{km}^2$	
$(\sigma_1^{\mathrm{obs}} = 264.66\,\mathrm{km}^2)$		$(\sigma_2^{\mathrm{obs}} = 246.00\,\mathrm{km}^2)$	
$T_1^{\mathrm{obs}} = 1969.72$		$T_2^{\mathrm{obs}} = 2006.31$	

$$A_2 = A_1\left(1 + f\left[T_2 - T_1\right]\right), \tag{S1}$$

where A_i are the total glacier area and T_i is the representative year of inventory i. From this equation, one can derive fractional and absolute regionwide area change rates, f and r:

$$f = \frac{A_2 - A_1}{A_1\left(T_2 - T_1\right)}, \tag{S2}$$

$$r = fA_1 = \frac{A_2 - A_1}{T_2 - T_1}. \tag{S3}$$

Similarly to Equation (S1), we write glacier area from each portion j of inventory i recalculated to the representative year with its own fractional change rate f_{ij}:

$$\begin{aligned} A_{ij}^{T_i} &= A_{ij}\left(1 + f_{ij}\left[T_i - t_{ij}\right]\right) = \\ &= w_{ij}S_i\left(1 + f_{ij}\left[T_i - t_{ij}\right]\right), \end{aligned} \tag{S4}$$

or if rewriting individual fractional area change rates as deviations from the regionwide rate, $f_{ij} = f + \Delta f_{ij}$:

$$\begin{aligned} A_{ij}^{T_i} &= w_{ij}S_i\left(1 + \left[f + \Delta f_{ij}\right]\left[T_i - t_{ij}\right]\right) = \\ &= w_{ij}S_i + w_{ij}\left(T_i - t_{ij}\right)fS_i + w_{ij}\left(T_i - t_{ij}\right)\Delta f_{ij}S_i. \end{aligned} \tag{S5}$$

The total glacier area is the sum of these recalculated

area portions:

$$
\begin{aligned}
A_i &= \sum_j A_{ij}^{T_i} = \\
&= \underbrace{\sum_j w_{ij}}_{1}\ S_i + \underbrace{\sum_j w_{ij}\,(T_i - t_{ij})\ fS_i}_{0 \text{ by construction}} + \sum_j w_{ij}\,(T_i - t_{ij})\,\Delta f_{ij} S_i = \\
&= S_i \left(1 + \sum_j w_{ij}\,[T_i - t_{ij}]\,\Delta f_{ij}\right).
\end{aligned}
\tag{S6}
$$

Note that the f term is 0, meaning that simple area-weighted averaging for the representative year already includes the correction for area changes that occured during $T_i - t_{ij}$, under the assumption that the fractional changes were identical among all area portions A_{ij} (i.e. if $\Delta f_{ij} = 0$).

Plugging Equation (S6) into (S2) and (S3) closes the system of equations. The only 'unknown' left is the Δf_{ij} term, $\sum_j w_{ij}\,(T_i - t_{ij})\,\Delta f_{ij} = (\star)$. Generally speaking, setting $(\star) = 0$ is a justifiable assumption:

(i) The large longitude and latitude ranges of almost all area portions in WGI and RGI, covering a wide range of climates, suggest $\Delta f_{ij} \approx 0$ and hence $(\star) \approx 0$.

(ii) $(\star)$ is the weighted covariance of $T_i - t_{ij}$ and Δf_{ij}. There is no good reason to assume that the image timing is correlated with the glacier area change rates as it is usually governed by logistics (for aerial campaigns) or cloud cover (for satellite acquisitions), thus $(\star) \approx 0$.

Nevertheless, instead if ignoring $(\star)$, we implemented a two-stage resampling procedure to estimate f and r. First, we derive an initial guess of f—f^{guess} with $\Delta f_{ij} = 0$. Then, we use this estimation to construct a pessimistic $\sigma_{\Delta f_{ij}}$ and rerun the resampling one more time to show that it does not affect our trend reevaluation considerably.

To estimate f and r as well as their uncertainties, we run a Monte-Carlo loop of 100 000 iterations. In Stage 1, in each iteration, we sample $K_i^{\text{eff}} = 1/\sum_j w_{ij}^2$ [5] years with replacement $\sim$ Categorical $(w_{i1}, \ldots, w_{iM_i})$ to account for uncertainties in assigning one representative year to a multi-year inventory, calculate T_i from the years sampled, sample $S_i \sim \mathcal{N}\left(S_i^{\text{obs}}, \sigma_i^{2\,\text{obs}}\right)$, set $\Delta f_{ij} = 0$, plug everything into Equations (S6, S2, S3) and calculate f and r. The averaged f from Stage 1 is then our f^{guess}.

In Stage 2, we repeat the same procedure, but instead of setting $\Delta f_{ij} = 0$ we sample $\Delta f_{ij} \sim \mathcal{N}\left(0, |f^{\text{guess}}|^2\right)$, allowing for the extremes of $f \pm 1.96f$ for all individual portions at the 95% coverage, which we consider extremely pessimistic, especially taking **(i)** and **(ii)** into account.

The results are presented in Supplementary Table 2. Taking into account the pessimistic Δf_{ij} widened the 95%-CI by $\approx$ 10%, suggesting that mapping error and representative year assignment dominate the uncertainty of the change rate. This result is in line with the numbers reported by Nuth et al. (2013) [1]: $-80\,\text{km}^2\,\text{a}^{-1}$ ($-77.97\,\text{km}^2\,\text{a}^{-1}$ without Kvitøya) lies within the 95%-CI; and if we recompute our average rate from the temporal spread of $\approx$ 37 to the 32-year one used in the original publication (which is somewhat arbitrary defined), we get $-77.55\,\text{km}^2\,\text{a}^{-1}$.

Supplementary Table 2 Historical trend reevaluation results.

Variable	Statistic	Stage 1	Stage 2
f, a^{-1}	Mean	−0.001936	−0.001933
	Median	−0.001926	−0.001921
	2.5$^{\text{th}}$ percentile	−0.002584	−0.002641
	97.5$^{\text{th}}$ percentile	−0.001356	−0.001299
$r, \text{km}^2\,\text{a}^{-1}$	Mean	−67.897	−67.819
	Median	−67.489	−67.301
	2.5$^{\text{th}}$ percentile	−91.325	−93.572
	97.5$^{\text{th}}$ percentile	−47.043	−44.943

If we take the glacier area change rate r from Stage 2 as the historical baseline and our modern estimate of $-227\,\text{km}^2\,\text{a}^{-1}$ as the point value—obtained after excluding polygons $< 2\,\text{km}^2$—while retaining the original $\pm 75\,\text{km}^2\,\text{a}^{-1}$ uncertainty band (derived from the full inventories, because the bootstrapping algorithm for total area uncertainty estimation does not permit filtering out individual polygons), then the 95%-CI of the acceleration factor we report is [2.03; 5.54] with the mean of $\times 3.48$ and the median of $\times 3.37$, allowing us to confidently claim at least two times accelerated glacier area loss in Svalbard, with $\times 3.4$ being the most likely estimate. Note that this 95%-CI is conservative due to the conservative estimates of mapping uncertainties σ_1^{obs} and σ_2^{obs}, the assumed independence between S_1 and S_2, the pessimistic choice of Δf_{ij} and the fact that the $\pm 75\,\text{km}^2\,\text{a}^{-1}$ spread still includes small-polygon contribution.

Validation against calving front datasets. To complement the validation, we compared our results against an expert-made (manual digitisation) calving front database by Moholdt et al. (2021) [6] and the deep-learning-based one by Li et al. (2024) [7], providing a completely independent evaluation of our method within the study period.

First, we compared calving front position change rates in 2016–2024, extracted from our annual inventories and

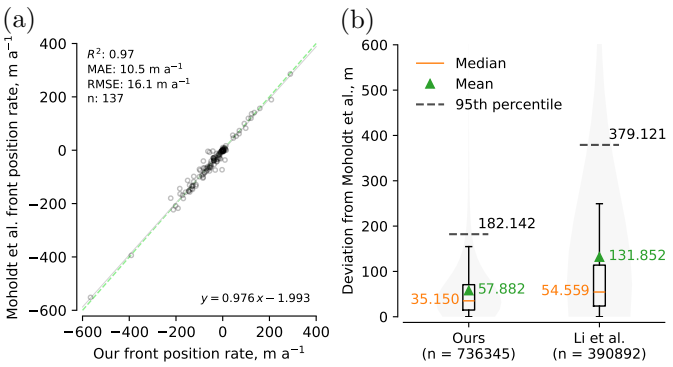

Supplementary Fig. 1 Calving front mapping validation: a comparison of calving front position rate derived from our dataset and Moholdt et al. (2021) [6] in 2016–2024, and **b** distance deviation as calculated from Moholdt et al. (2021) [6] to our dataset, 2016–2024 vs. the Li et al. (2024) [7] dataset, 2016–2022.

Moholdt et al. (2021) [6] and found an excellent match (R^2 = 0.97; Supplementary Figure 1a) on par with that reported by Li et al. (2024) [7] for 2008–2022 (R^2 = 0.98).

We also compared the distance deviations between the manually digitised calving fronts from Moholdt et al. and our results by sampling points from the Moholdt et al. traces every 10 m and computing the distance to our outlines for each year. In this case, we did not filter out any traces and did not take any subsets of the area of interest. We computed a similar metric to compare Li et al. against Moholdt et al. in the same terms; for that, we selected the traces from Li et al. that are closest in time to the manually created ones and only within a ±15-day window, overlayed the manually created traces with the fjord masks and computed the distance deviations in the same manner. Note a more exclusive protocol in the latter case. Overall, we found superior correspondence between our results and the manually delineated calving fronts, as well as approximately twice as good (58 m vs. 132 m errors on average) ability to detect calving front positions at the end of the ablation season compared to the deep learning baseline (Supplementary Figure 1b). Part of the observed uncertainty in the distance deviations is explained by slight temporal mismatches between the three products.

Austfonna, Basin-7 surge. In our analysis for the 2016–2024 epoch, a notable positive anomaly was observed in the area change of Austfonna's Basin-7. Our annual outlines show the terminus advancing by approximately 1.2 km between 2019 and 2021, consistent with the velocity anomaly noted, but not catalogued, in the most comprehensive surge inventory known to us of Strozzi et al. (2024) [8]. The same event is also marked in the calving front time series of Li et al. (2024) [7].

Additional evidence for active surging comes from the Sentinel-1 backscatter time series (Supplementary Figure 2), where a marked increase in radar return—commonly associated with widespread crevassing [9, 10]—co-occurs with the frontal advance. Although this surge has therefore been hinted at in previous work, it is still absent from the surge datasets to date not based on geometry tracking [10–13].

This finding revalidates the utility of annually updated glacier inventories, not as a superior method, but as a valuable complementary tool that can enhance more traditional methods for surge detection.

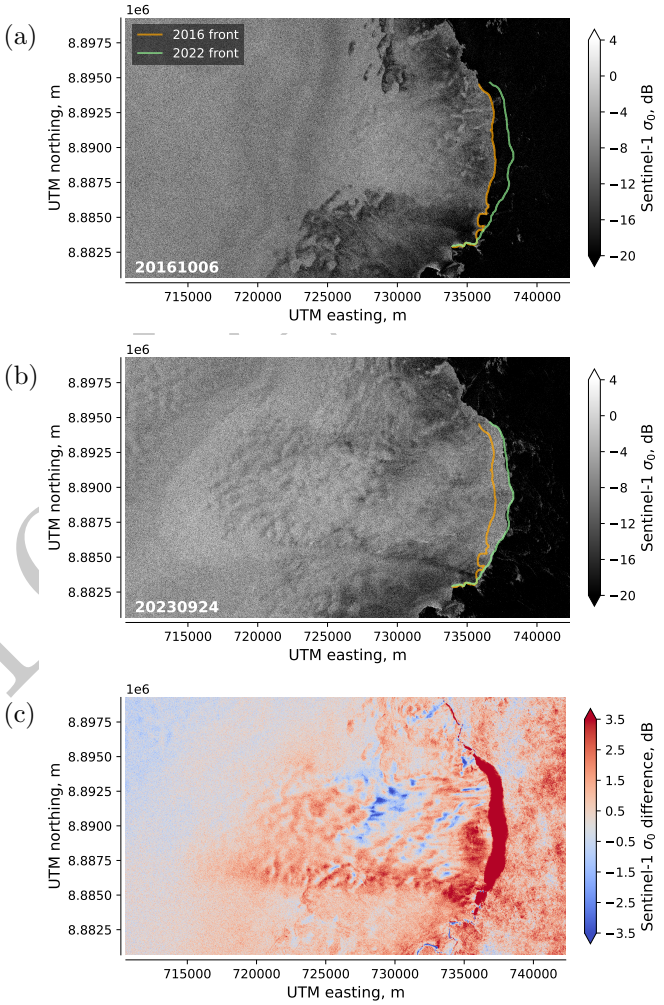

Supplementary Fig. 2 Glacier surge of Austfonna, Basin-7: a a Sentinel-1 image from Autumn 2016, **b** an image from Autumn 2023 and **c** backscatter difference of two averaged images from 2019–2022 and 2016–2018. An animated version is available at `https://figshare.com/s/caf969067065a0d968ae`. Copernicus Sentinel data 2016–2025.

Supplementary Figures and Tables

Supplementary Table 3 Validation performance of ICEmapper in different training settings.

Feature set	Pooling	IoU[a]	
		Patch-wise	Pixel-wise
GRD	max	0.875	0.960
GRD	time-weighted	0.877	0.962
RTC	time-weighted	0.883	0.962
InSAR	time-weighted	0.847	0.939
GRD+InSAR	time-weighted	**0.893**46	**0.963**
RTC+InSAR	time-weighted	0.893**23**	0.962

[a] The best IoU values are in bold.

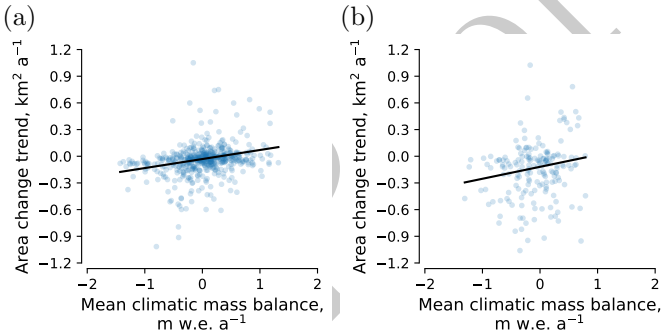

Supplementary Fig. 3 Glacier area change rate against climatic mass balance [14]: **a** for land-terminating ($r_s = 0.30$, p-value < 0.05) and **b** for tidewater ($r_s = 0.14$, p-value ≈ 0.05) glaciers $> 2\,\mathrm{km}^2$ in the RGI7.0–2016 epoch averaged per glacier.

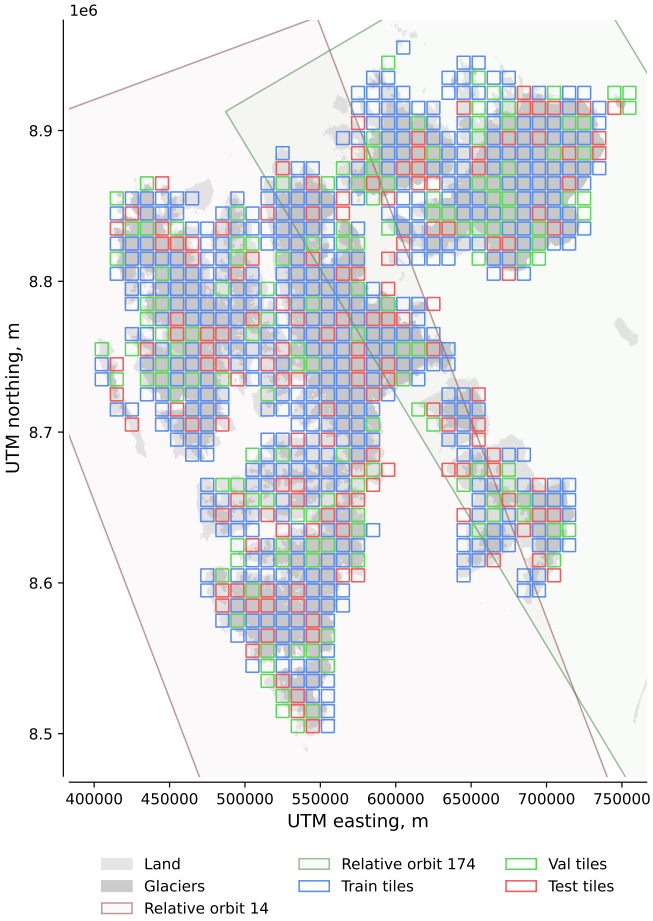

Supplementary Fig. 4 Study area overview. Tile sizes are reduced for visualisation purposes. The glacier outlines are taken from Kohler et al., 2021 [15].

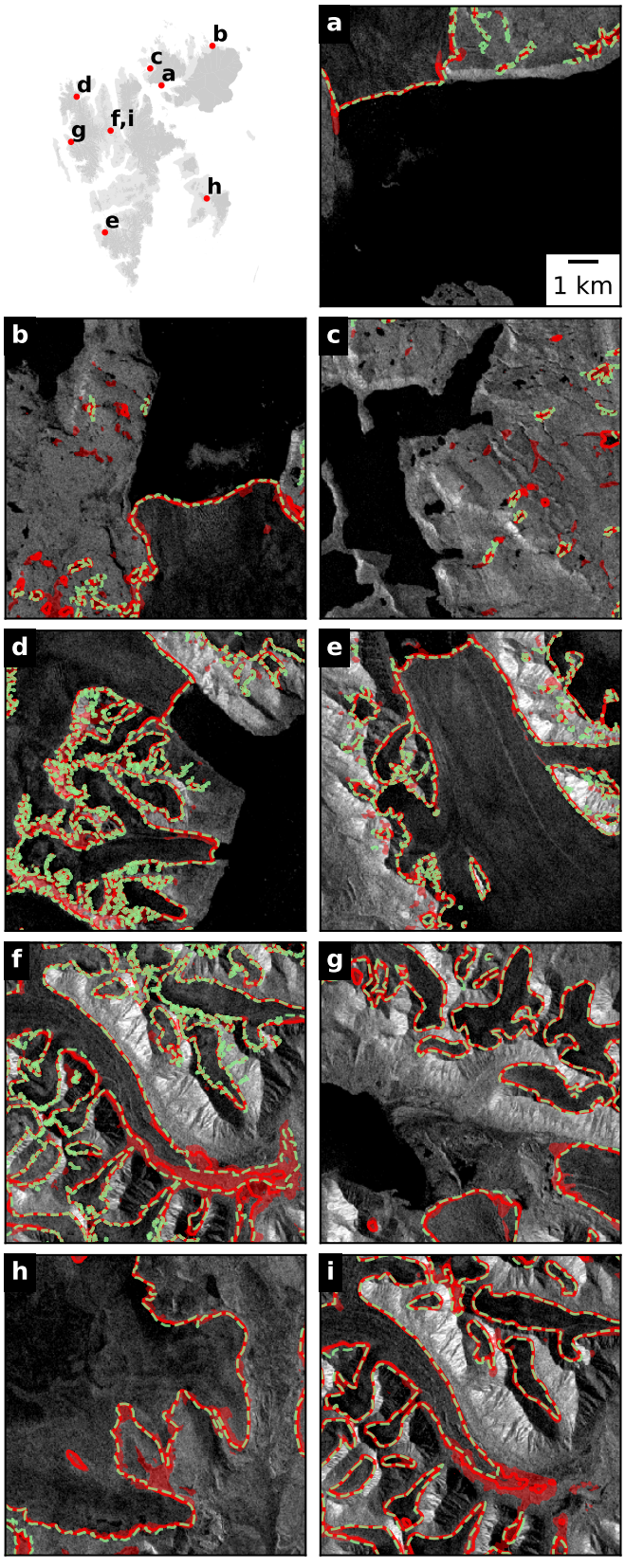

Supplementary Fig. 5 Closeups of test classification results: from **a, b, c** 2016, **d, e, f** 2017 and **g, h, i** 2020. The 95%-confidence bands are shown as red transparent areas. Copernicus Sentinel data 2016, 2017 and 2020.

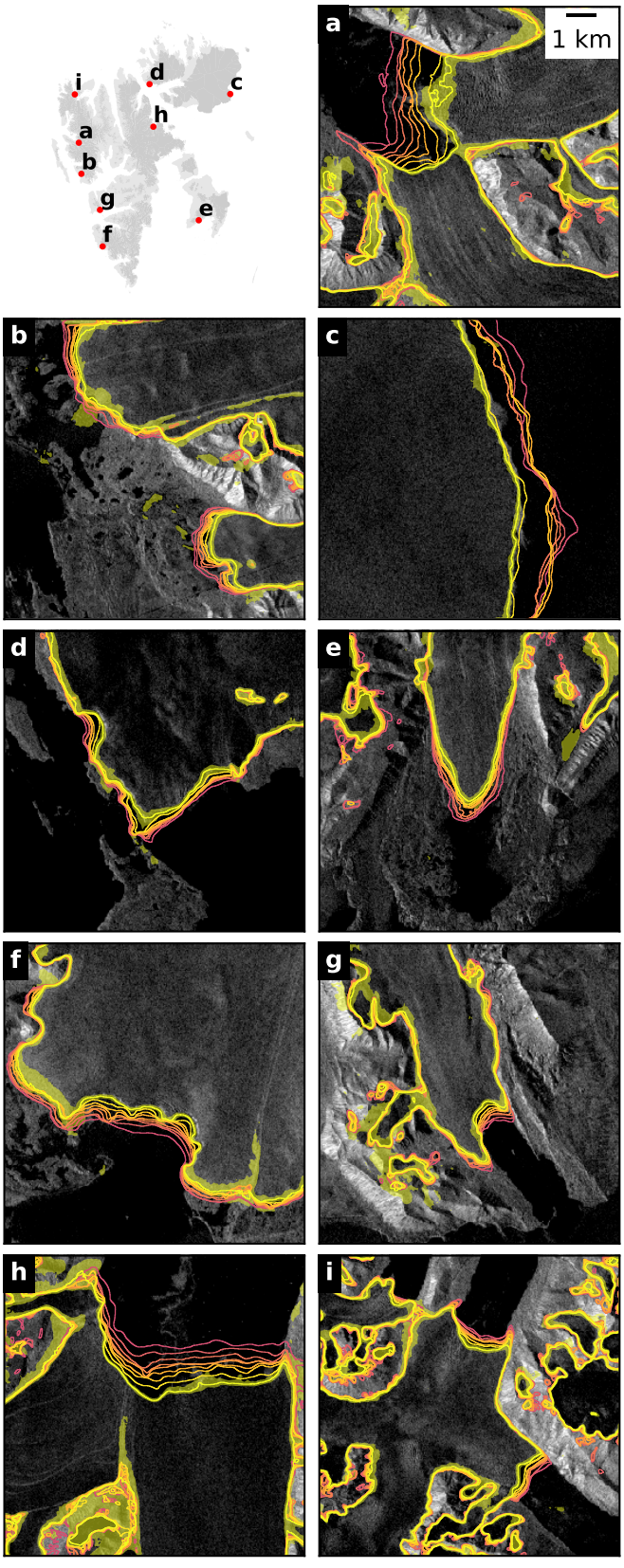

Supplementary Fig. 6 Significant changes in glacier outlines found at the pixel level. The 95%-confidence bands are shown as yellow transparent areas. For clarity, confidence bands are presented only for 2024. Copernicus Sentinel data 2024.

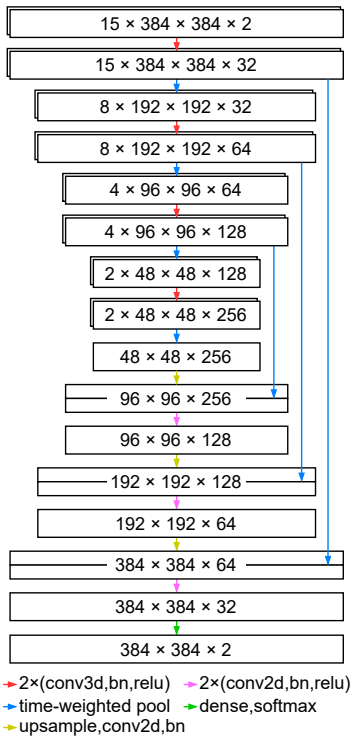

Supplementary Fig. 7 Intensity-Coherence-Evolution-mapper (ICEmapper). Boxes and numbers in them represent tensors and their shapes in the [time×]height × width × channels format, and arrows indicate operations.

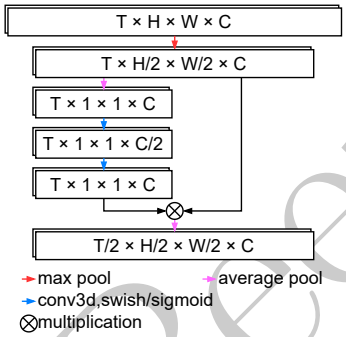

Supplementary Fig. 8 Time-weighted pooling block. Text in boxes represents tensor shapes in the time × height × width × channels format, and arrows indicate operations and data flow.

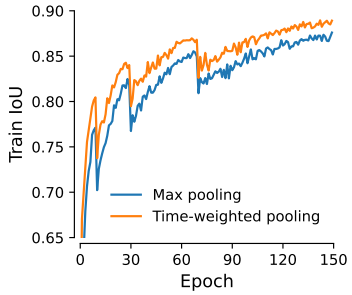

Supplementary Fig. 9 Train IoU dynamics for ICEmapper trained with GRD only data with max pooling and time-weighted pooling.

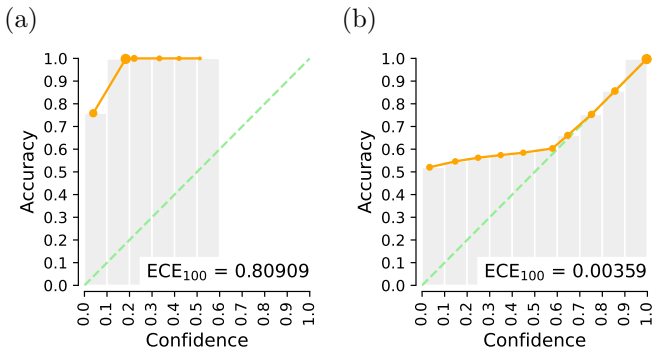

Supplementary Fig. 10 Reliability diagrams: a before and **b** after confidence calibration. ECE stands for expected calibration error. Green lines indicate the ideal calibration case. The marker sizes are proportional to the number of pixels within a bin.

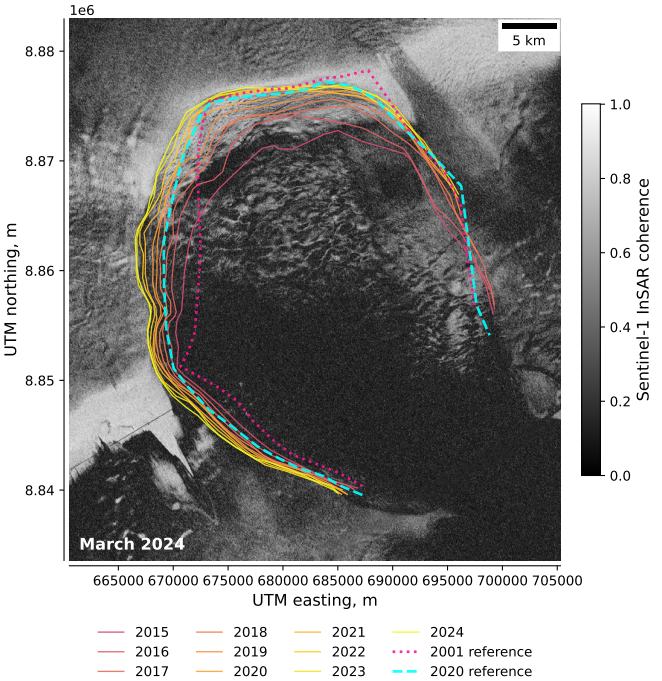

Supplementary Fig. 11 Surge-induced expansion of Austfonna, Basin-3 dynamic extent observed in InSAR coherence images. The 2020 reference ice divides are from Kohler et al., 2021 [15], and the 2001 reference ice divides are from RGI7.0 [4]. Copernicus Sentinel data 2024.

References

1. Nuth, C. *et al.* Decadal changes from a multi-temporal glacier inventory of Svalbard. *The Cryosphere* **7,** 1603–1621. https://tc.copernicus.org/articles/7/1603/2013/ (2013).
2. Hagen, J. O., Liestøl, O., Roland, E. & Jørgensen, T. *Glacier atlas of Svalbard and Jan Mayen* http://hdl.handle.net/11250/173065 (Norwegian Polar Institute, 1993).
3. World Glacier Monitoring Service. *World Glacier Inventory, Version 1* https://doi.org/10.7265/N5/NSIDC-WGI-2012-02.
4. RGI Consortium. Randolph Glacier Inventory—A Dataset of Global Glacier Outlines, Version 7. *Boulder, Colorado USA. NSIDC: National Snow and Ice Data Center.* (2023).
5. Kish, L. *Survey sampling* (John Wiley & Sons, New York, 1965).
6. Moholdt, G., Maton, J., Majerska, M. & Kohler, J. *Annual frontlines of marine-terminating glaciers on Svalbard* 2021. https://data.npolar.no/dataset/d60a919a-9cc8-4048-9686-df81bfdc2338.
7. Li, T. *et al.* A high-resolution calving front data product for marine-terminating glaciers in Svalbard. *Earth System Science Data* **16,** 919–939. https://essd.copernicus.org/articles/16/919/2024/ (2024).
8. Strozzi, T., Cantus, O. & Santoro, M. *Glaciers_CCI project: ERS-1/2 C-band data over Svalbard* Project Report (GAMMA Remote Sensing AG, Switzerland, Oct. 2024).
9. Leclercq, P. W., Kääb, A. & Altena, B. Brief communication: Detection of glacier surge activity using cloud computing of Sentinel-1 radar data. *The Cryosphere* **15,** 4901–4907. https://tc.copernicus.org/articles/15/4901/2021/ (2021).
10. Kääb, A., Bazilova, V., Leclercq, P. W., Mannerfelt, E. S. & Strozzi, T. Global clustering of recent glacier surges from radar backscatter data, 2017–2022. *Journal of Glaciology* **69,** 1515–1523 (2023).
11. Koch, M., Seehaus, T., Friedl, P. & Braun, M. Automated Detection of Glacier Surges from Sentinel-1 Surface Velocity Time Series—An Example from Svalbard. *Remote Sensing* **15.** ISSN: 2072-4292. https://www.mdpi.com/2072-4292/15/6/1545 (2023).
12. Harcourt, W. D. *et al. Svalbard Surge Database 2024 (RGI2000-v7.0-G-07)* (Zenodo, Apr. 2025). https://doi.org/10.5281/zenodo.15240754.
13. Mannerfelt, E. S., Schellenberger, T. & Kääb, A. Tracking glacier surge evolution using interferometric SAR coherence—examples from Svalbard. *Journal of Glaciology* **71,** e43 (2025).
14. Van Pelt, W. *et al.* A long-term dataset of climatic mass balance, snow conditions, and runoff in Svalbard (1957–2018). *The Cryosphere* **13,** 2259–2280. https://tc.cope rnicus.org/articles/13/2259/2019/ (2019).
15. Kohler, J., Lith, A. & Moholdt, G. *Svalbard glacier inventory based on Sentinel-2 imagery from summer 2020* 2021. https://doi.org/10.21334/npolar.2021.1b8631bf.